Control of optical nanometer gap shapes made via standard lithography using atomic layer deposition

Jiyeah Rhie
Dukhyung Lee
Young-Mi Bahk
Jeeyoon Jeong
Geunchang Choi
Youjin Lee
Sunghwan Kim
Seunghun Hong
Dai-Sik Kim

Control of optical nanometer gap shapes made via standard lithography using atomic layer deposition

Jiyeah Rhie,[a,*] Dukhyung Lee,[a] Young-Mi Bahk,[b] Jeeyoon Jeong,[a] Geunchang Choi,[a,†] Youjin Lee,[a] Sunghwan Kim,[a] Seunghun Hong,[c] and Dai-Sik Kim[a]
[a]Seoul National University, Center for Atom Scale Electromagnetism, Department of Physics and Astronomy, Seoul, Republic of Korea
[b]Incheon National University, Department of Physics, Incheon, Republic of Korea
[c]Seoul National University, Astronomy and Institute of Applied Physics, Department of Physics and Astronomy, Seoul, Republic of Korea

Abstract. Atomic layer deposition is an efficient method for coating a few nanometer-thick alumina over a wafer scale. This method combined with the standard photolithography process was presented to fabricate metallic nanometer gaps that optically act in terahertz regimes. However, the cross-sectional view of the gap shape of the metal–insulator–metal nanogap structure varies depending on the conditions from the stepwise procedure. In specific, selecting photoresist materials, adding ion milling and chemical etching processes, and varying metal thicknesses and substrates result in various optical gap widths and shapes. Since the cross-sectional gap shape affects the field enhancement of the funneled electromagnetic waves via the nanogap, the control of tailoring the gap shape is necessary. Thus, we present five different versions of fabricating quadrangle-ring-shaped nanometer gap arrays with varying different kinds of outcomes. We foresee the usage of the suggested category for specific applications. © The Authors. Published by SPIE under a Creative Commons Attribution 3.0 Unported License. Distribution or reproduction of this work in whole or in part requires full attribution of the original publication, including its DOI. [DOI: 10.1117/1.JMM.17.2.023504]

Keywords: atomic layer deposition; standard lithography; nanometer gap; cross-sectional gap shape; field enhancement.

Paper 17118 received Aug. 16, 2017; accepted for publication Mar. 29, 2018; published online May 3, 2018.

1 Introduction

Nanometer-gap structures are widespread in nanoplasmonics, including nanoantennas,[1,2] which can be applied to surface-enhanced Raman scattering (SERS) sensing,[3,4] biomaterial sensing,[5,6] nonlinear behaviors,[7,8] optical circuits,[9] and optical trappings.[10,11] From visible lights to gigahertz waves, studies have shown that light waves can funnel through a nanometer-gap enhancing electromagnetic fields.[12–15]

Since nanogap arrays in metallic films reveal strong, resonant field enhancement (FE) of electromagnetic fields, studies in nanotechnology have shown a facile and high-efficiency way to fabricate specific designs. Here, a few nanometer-gap width strongly affects the optical property of the whole structure, for example, the FE factor increasing as the gap width decreases.[16,17] Nanolithography[18–21] based on hydrogen silsesquioxane (HSQ) by e-beam lithography and shadow masking lithography[22–24] has been used in fabricating sub-10-nm gap arrays to increase the FE factor for specific applications. The established techniques have advantages for fabricating closely packed-nanogap arrays with freedom in pattern designs. However, the indirect approaches and a low throughput of serial milling on HSQ templates by e-beam lithography bring out the limitations of achieving well-defined gap widths in millimeter or centimeter scale, which is inadequate for a use of nanoantennas in terahertz and gigahertz frequency regimes. On the other hand, the combination of glanced-angle deposition and shadow masking lithography on patterned materials enables fabrication of nanogap arrays on a large scale, such as a few millimeter-scale square area with direct patterning technique,[25] yet lacks one nanometer-scale control since the gap width of the nanogap arrays depends on the thickness of the deposited metallic film and the depositing angle.

The combination of UV lithography and atomic layer deposition (ALD) developed by Chen et al.[26] shows the well-defined nanogap arrays over a wafer scale by utilizing a few nanometer-thick alumina spacers[27,28] in between the metallic film. The spacer is deposited directly on the patterned film with high controllability and, subsequently, the metallic film is deposited to form the spacer as the nanogaps. Eventually, the nanogaps appear as the outlines of the ring-shaped gap arrays as in Figs. 1(a) and 1(b). These lines can be 1-mm and even 1-cm long depending on the size of the patterned metallic structures via the photomask [see l_x and l_y in Fig. 1(b)]. The perimeters of the outlines are long enough to enable the enhanced field in the nanogaps to function in terahertz and gigahertz frequency regimes.

Although an adequate gap width of the nanogap can be made by ALD, the resulting cross-sectional gap shape is not repeatable in terms of the different thickness of the metallic film and cross-sectional profiles of the patterned metallic film resulting from the conditions of the photolithography and lift-off processes. Since the localized enhancement varies depending on the metallic film thickness and the tapered angle of the metallic film at the nanogap,[29,30] the fabrication techniques should be classified by gap shape among the possible results and refine each stepwise procedure.

The gap shape plays an even more important role when it comes to applications in specific fields due to the different cross-sectional enhancement area in the gap between metallic structures. For instance, V-groove gaps are used for plasmonic light confinement.[31,32] In particular, the spot-like dimension of the cross-sectional enhancement area is

*Address all correspondence to: Jiyeah Rhie, E-mail: trhie@snu.ac.kr

†Present Address: Sungkyunkwan University, Department of Energy Science, Suwon, Republic of Korea
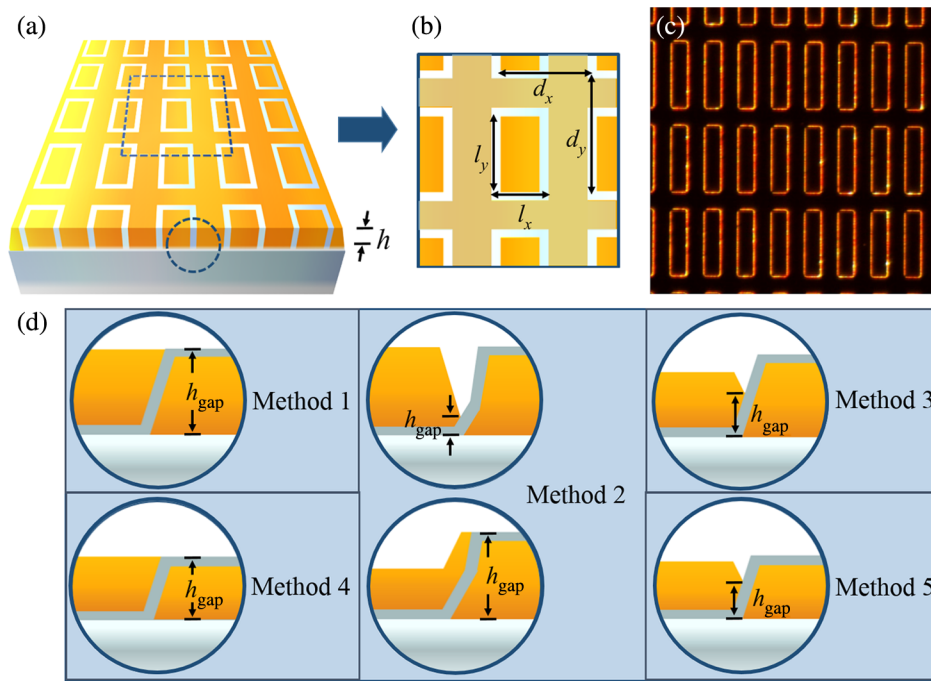
Fig. 1 MIM nanometer gap structure: (a) a perspective view and (b) a top view of schematic diagrams of the nanogap sample. The alumina-outlines (w) of rectangular-ring shapes (l_x, l_y) are arranged in certain periodicities (d_x, d_y) in between metallic films of thickness, h. The spacing between each rectangular arrays is l_x. (c) Transmitted optical microscope image of a nanogap sample (l_x: 10 μm, l_y: 40 μm, d_x: 20 μm, d_y: 50 μm, w: 5-nm gap, and h: 150 nm) made by method 1. (d) Cross-sectional schematics of MIM nanometer gap and corresponding gap thickness (h_{gap}) of each method. The thickness of the alumina layer determines the width (w) of the nanogap in all methods.

capable to trap one or two particles by enhanced optical trapping at the nanoantenna without stacking more particles.[33,34] On the contrary, the nanogap structures with a high-aspect ratio composing a line-like cross-sectional enhancement area within the gap have simplified FE volume in the fields of nanoelectrodes,[35] optical circuits,[36] and optical nonlinearity measurements[8,37] compared with other gap shapes. In addition, the feature of the cross-sectional geometry is adjustable to fill a layer of particles in between the metallic structure.[35,38,39] Therefore, having complete control over the gap geometry is crucial for applications in diverse fields.

In this paper, we improve the atomic layer lithography to diversify gap shapes and film thicknesses. The optical gap width and angle can be controlled by selecting photoresist types and thickness, adding ion beam etching and chemical etching processes, and varying metal thicknesses and substrates. The basic structures of the nanometer gaps are shown in Fig. 1, and alumina spacers grown by ALD are sandwiched between metallic films. As described in Fig. 1(d), the gap thickness (h_{gap}) and gap shapes vary depending on the five versions of our fabrication methods. The top view of the nanometer gaps shows the width (l_x) and the length (l_y) of the rectangular-ring arrays. These gap rings are separated by l_x in both x- and y-directions forming antennas at terahertz frequencies.[17,26,40]

2 Fabrication Procedure

Each method is basically used to form sub-10-nm-wide gaps between the metals carried out by photolithography, metal deposition, ALD, and the exfoliation processes (Fig. 2).

The first step is to pattern the first metal frame by photolithography, making a rectangular hole array in a metallic thin film. In the photolithography process, we designed the Cr photomask to make the in-plane dimensions of method 1 to 5 as the patterns of 10 μm(l_x) × 10 μm(l_y), 10 × 40 μm, 50 × 50 μm, and 3 mm × 5 mm. This is intended to show that the samples can be made regardless of the in-plane dimensions. The second step is to coat a few nanometer-thick insulator (alumina) layer over the whole structure by ALD. The third step is to deposit second metallic films that are for filling the hole of the first metallic frame and forming metal–insulator–metal (MIM) nanogap structures. Last, we exfoliate the unnecessary metallic film using a tape or a chemical etchant to expose nanogaps for optical purposes.

2.1 Step 1: First Metal Frame

The first metal frame formation includes the photolithography process, metal deposition, and subsequent lift-off. On a bare substrate, a metallic film with an adhesion layer (3 nm of chromium) is patterned using standard photolithography (AZ5206E and AZ5214E, image reversal) in methods 1, 2, and 3. On the other hand, the patterned photoresist or the patterned sacrificial layer is used as an ion beam etching mask to design the first metallic frame with bare metallic films in methods 4 and 5. Since the formation of all methods are based on photolithography for different resulting gap shapes, the demonstrations of the appropriate thickness and type of the photoresist with optimized conditions for each method are necessary.
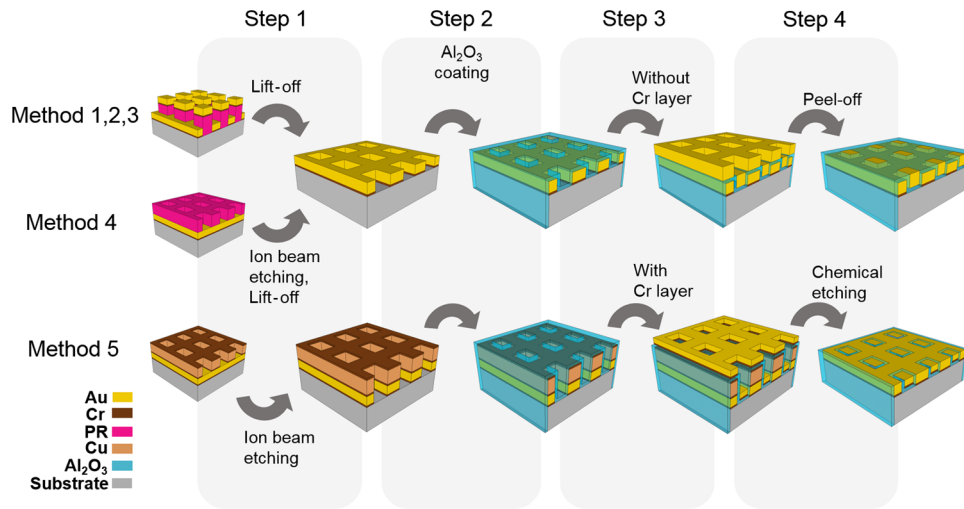
Fig. 2 Schematic illustrations of stepwise procedures of the five methods consisting of four steps: first metallic frame formation, ALD process, second metallic film deposition, and the exfoliation process. At step 1, the first metallic frame is formed by photolithography, metal deposition, and lift-off in methods 1, 2, and 3. Photoresist pattern (pink) is used as a shadow mask for ion beam etching, and after the lift-off, the first metallic frame is formed in method 4, while a metallic pattern is used for a shadow mask in method 5.

2.1.1 Step 1: Photoresist and substrates

The low line edge roughness of the metal frame after lift-off is a prerequisite for achieving a consistent gap width along hundreds of a micrometer length. When the sidewalls of the photoresist are undercut shape, lift-off is easier without remaining residues and prevents the resist sidewalls from being coated, which eventually make the line edges of the metallic patterns clearer. Therefore, photoresist of the right type and height should be chosen for the very specific gap shape one desires. Types of photoresist determine the metal profile after lift-off processes, and there is an optimal photoresist height for the chosen thickness of the metal. For this reason, we used commercial photoresists, AZ5214E and AZ5206E, an image reversal type. In general, an image reversal type ends up in an inverted trapezoidal shape much in the same fashion as a negative type, which shows straight line metal edges with graded sidewall profiles.

After selecting the photoresist type, we define photolithography conditions for patterned metal films with desired edge angles. The conditions of the photoresist height of AZ5214E and AZ5206E were targeted to 1.2 and 0.6 μm, respectively. The recipes of both image reversal type photoresists are revealed in this section depending on silicon, sapphire, quartz, and gold film. When each condition of this process is optimized, the deposited metal cliffs can have a clearer edge with a specific sidewall angle.

For target metal thickness of 300 to 400 nm, AZ5214E photoresist is well suited by following a rule of thumb in photolithography; the resist thickness should be at least three times greater than the metallic film thickness. The photoresist patterns are made on bare substrates (sapphire, quartz, and silicon) and on metallic films. The sample is cleaned with acetone, isopropanol, and deionized water and spin-coated at 4000 rpm for 60 s, followed by soft-baking at 90°C for 90 s. For sapphire or quartz substrates, Hexamethyldisilazane is spin-coated at 4000 rpm for 60 s before spin-coating the photoresist in order to promote adhesion between the photoresist and the substrate. We used 365-nm i-line mercury arc lamp in a mask aligner (Karl Süss

MJB-3, Süss MicroTec) for mask exposure, where the sample is illuminated through Cr mask with an exposure dose of 140 mJ/cm^2. Then, the sample was postbaked at 115°C for 85 s and exposed to UV lamp again without the mask for with exposure dose of 300 mJ/cm^2. Finally, we developed the sample in MIF (Metal Ion Free) 300 developer (AZ Electronic Materials) for 30 s. The development time depends on pattern size: 10 μm(l_x) × 10 μm(l_y) takes 90 s, 50 μm × 50 μm takes 30 s, and 3 mm × 5 mm takes 20 s. AZ5214E is used for methods 2, 3, and 5 (see Table 1). In the case of method 5, although the maximum thickness of the first metallic film is lower than the case of methods 1 and 4, a 185-nm-thick sacrificial layer is added on top of the metallic film, which is suitable to use AZ5214E.

Meanwhile, AZ5206E is suitable for smaller metal thickness of 150 to 200 nm used for methods 1 and 4. The recipe is similar but the reversal bake time, and the first and the second exposure dose are different. The UV exposure dose with a Cr mask is 120 mJ/cm^2, the reversal bake time is 120 s at 115°C, and the second UV exposure dose without the mask is 800 mJ/cm^2; other conditions are the same as used in photoresist AZ5214E. The samples are developed in MIF 300 for 3 s and then gently soaked in deionized (DI) water without shaking or sonication. This is repeated once more until the patterns appear and it is distinguishable by looking through the optical microscope. If the sample is developed for 6 to 7 s without this interruption, then the photoresist might vanish before the patterns emerge.

During the second UV exposure without a mask, the entire resist film is exposed to make the resist areas—up to now, the unexposed areas—developable. The exposure dose should be high enough to fully transmit through the bottom of the resist transferring a positive type to image reversal type. For this reason, the second exposure dose is longer for the thick resist case. Moreover, the thickness of the resist film also affects the develop time. A thick resist film (5214E) is developed longer than the thinner one, AZ5206E. The second exposure dose is 300 mJ/cm^2 for the AZ5214E case while the case for AZ5206E is 800 mJ/cm^2 because the develop

Table 1 Fabrication methods.

	Procedure (units)	Method 1	Method 2	Method 3	Method 4	Method 5
Step 1	Photoresist	AZ5206E	AZ5214E	AZ5214E	AZ5206E	AZ5214E
	First metal (nm)	150 to 200	300 to 400	>200	<120	<100
Step 2	Al2O3 (nm)	5	5	5	5	5
Step 3	Second metal (nm)	150 to 200	200 to 370	>150	<120	<100
Step 4	Exfoliation	T	T	T	T	C
	Ion beam etching	X	X	X	O	O

Note: O means that the process is carried out. X means that the process is absent. T means the process using an adhesive tape. C means the process using chemical etchant. The inequality of the charts ($<$, $>$) shows the minimum and/or the maximum of the metal thickness of each methods.

time is long enough to erase the unwanted photoresist with a reversal bake time of 85 s. However, the thinner photoresist develop requires only 7 s in MIF 300. The thinner the resist thickness is, the longer the baking time is, to maintain the cross-sectional sidewall. Therefore, increasing the reversal bake time from 85 to 120 s and the second UV expose dose from 300 to 800 mJ/cm^2 are necessary for a short-time development.

2.2 *Step 2: Atomic Layer Deposition*

A thin Al_2O_3 layer is coated on framed metal by ALD at 220°C (NCD Co., Lucida™ D series). ALD is an unusual type of chemical vapor deposition, in which the two precursors react at the surface in a sequential manner by nonoverlapping pulses and there are no precursors remaining in the chamber by the time the next pulse begins. The precursors are gaseous species and they are injected in the chamber reacting with the surface materials in a self-limiting way. Consequently, the thickness after a single injection of the two precursors, referred as a single cycle, is controlled by the nature of the precursor–surface interaction.[41,42] Therefore, the thickness of the conformal thin film can be controlled by changing the number of the repeated cycles in angstrom scale.

In this study, trimethylaluminum and H_2O vapor are sequentially pulsed through the ALD chamber in 1.7 Torr for 0.1 s each and N_2 gas is used to purge the chamber in 1.56 Torr for 10 s after each injection. The total thickness of the Al_2O_3 film is measured through cross-section image of field-emission scanning electron microscopy (FE-SEM), and the measured deposition rate for Al_2O_3 is 1.2 Å/cycle. These conditions are applied in all five methods to form a sub-10-nm dielectric gap in between the metallic film. Although this process is not a variable in determining gap shape, it is an essential step to make an MIM nanogap structure.

2.3 *Step 3: Second Metallic Film Deposition*

The second metallic film is deposited by an e-gun evaporator without a rotation to fill the hole of the first metallic frame and form MIM nanogap structure in a cross-sectional view. The metallic film without an adhesion layer is deposited in methods 1, 2, 3, and 4. On the other hand, a Cr 3-nm layer is evaporated before the metallic film deposition in method 5.

The existence of the adhesion layer is strongly related to the exfoliation process. The thickness of the second metallic film is the same or about 30 nm lower than the first metallic frame, which depends on the geometry of the edge of the first metallic frame (see Table 1).

2.4 *Step 4: Exfoliation Process*

The unnecessary metallic film is easily exfoliated using a tape to expose nanogaps for optical purposes, when the second deposition process does not include an adhesion layer (Cr layer) as in methods 1, 2, 3, and 4. Scotch tape is applied on the sample after step 3. The tape is attached to the unnecessary metallic film that is on top of the first frame and removes it, except the second deposited film that is plugged inside the hole of the first frame. The remaining sample contains the desired MIM nanogap structure, easily seen in cross-sectional views.

On the other hand, when the second metallic film includes the Cr layer, the chemical etchant is used to exfoliate the unnecessary films by dissolving the sacrificial layer as in method 5. The sacrificial layer, patterned metallic film (Cr/Cu/Cr), is a layer that is removed in the etching process. This layer separates the second metallic film: the unnecessary film that is on top of the sacrificial layer and the secondary film filled inside the first metallic film. The deposition of the Cr layer at step 3 enables the second metallic films to survive under the ultrasonic agitation for cleaning the undesired remains from the chemical etching on the sample.

Specifically, the sacrificial layer is deposited as Cr 5 nm– Cu 160 nm–Cr 20 nm. The 5 nm of Cr layer is at the interface between a bare Au film and the patterned Cu film to prevent Au–Cu alloy formation due to the heat during evaporation. The 160-nm Cu layer acts as a sacrificial layer in a chemical etchant, and the height is thick enough to expose a large cross-sectional area to the etchant even when the secondary Au film is deposited. Although the Cr mask itself can act as a single sacrificial layer, the Cr melting point is 1907 deg so that the deposition process of the Cr layer of 100 nm can heat the whole chamber from inside while evaporating, and the photoresist will become too rigid to be lifted off. For stripping the sacrificial layer, a pure amount of 8 ml of CR-7 (mixtures of perchloric acid and ceric ammonium nitrate, Cyantek) is diluted in 100 ml of DI water as a chemical

etchant, and the wet-etching process is carried out for about 24 min.

2.4.1 *Sample characterization*

The nanogap fabrication techniques using the chemical etching process is already well-known by the previous studies, and the uniformity of the gap in a millimeter-scale square area has been confirmed by scanning electron microscope (SEM) images and transmitted optical microscope images at low magnification.[12,13] To confirm the uniformity of the nanogap sample after the tape-peeling process, we observed a sample with field emission scanning electron microscopy at low magnification in Figs. 3(a) and 3(b). The in-plane dimension of 10- × 10-μm-squared loop alumina-line array is used for the SEM images to quantitatively confirm the uniformity around the nanogap after tape peeling. The cross-sectional images in Figs. 3(c) and 3(d) show that the nanogap is formed with the thickness of 230 nm and the width of 5 nm with an average sidewall angle as 76 deg. The yield of the sample after tape peeling is as high as the chemical etching process, as long as the sidewall angle of the patterned metallic film is higher than 70 deg. These images show that the nanogap structures are well covered in same structural dimensions over a millimeter-scale square area.

In addition, the topographic images of a sample after tape peeling and a sample after chemical etching are observed by atomic force microscopy (AFM) in Figs. 4(a) and 4(b). In both cases, the first metallic frame thickness is 15 nm higher than the thickness of the secondary metallic film to increase the yield of the nanogap structure. The two samples can be distinguished by different patterns, for instance, 10-μm × 10-μm-squared patterns for the tape-peeling case and 10-μm × 40-μm-patterns for the chemical etching case. The line profiles of Figs. 4(c) and 4(d) are obtained from the red-colored area in the corresponding topographic images of Figs. 4(a) and 4(b), respectively. The tape-peeled sample shows some defects the size of 8 to 15 nm near the nanogap line as in Fig. 4(c). The tilted view of the SEM image in Fig. 3(c) ensures that the defects occurred when splitting the connections of the secondary metallic layer at
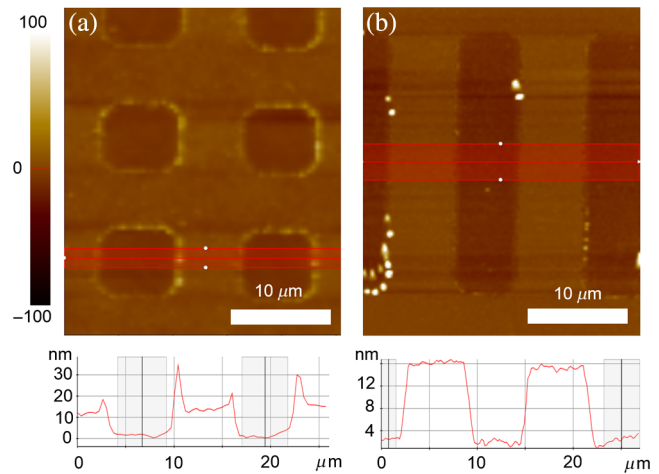

Fig. 4 AFM topographic images of nanogap sample (a) after tape peeling and (b) after chemical etching. The line profiles (c) after tape peeling obtained from the red-colored area of (a) and (d) after chemical etching obtained from the red-colored area of (b).

the gap line, separating it into the parts that are on the patterned frame and the portions that are plugged into the holes of the patterned frame. However, after etching, a part of the reacted material remaining as particles is observed at some of the gap lines, the contours of the squares [Fig. 4(b)]. The remaining can be removed by cleaning the sample again because the secondary metallic film contains an adhesion layer [see Fig. 9(b)]. The average surface roughness of the peeled surface is found to be 0.625 nm after chemical etching and 1.089 nm after tape peeling. These results show that the surface uniformity of the nanogap structure made by chemical etching is superior on the sample made by tape peeling, but both exfoliation processes are reliable because of the high yield.

3 Results

3.1 *Cross-Sectional View of the Nanogap Structures*

We investigated the influence of the different fabrication methods on MIM nanometer-gap structures in a cross-sectional
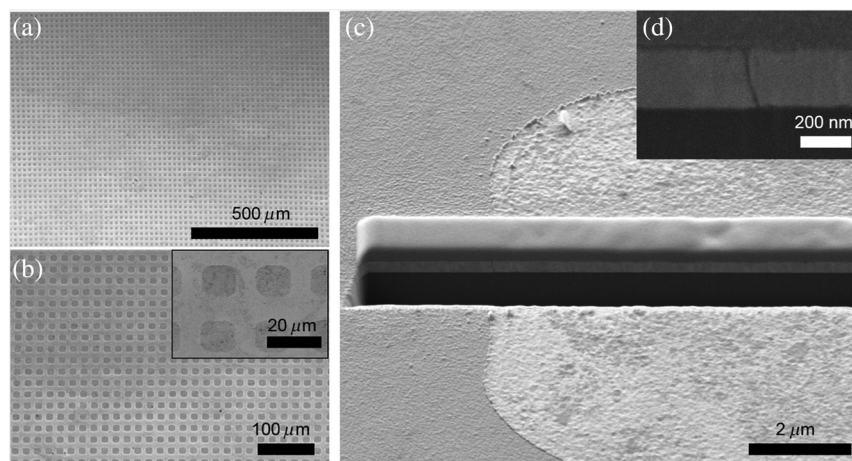

Fig. 3 (a) A top-view SEM image of nanogap sample after tape peeling at low magnification. (b) An enlarged image of (a). The inset shows the enlarged version of (b), showing a few 10- × 10-μm-squared loop of alumina line. (c) A tilted SEM image of a left side of the square loop. The Pt deposition layer is used for protecting the surface damage while etching the groove by focused ion beam. (d) A cross-sectional image of an enlarged image of (c), focused on the nanogap.

Table 2 Parameters of the nanogap structures.

Parameters (units)	Method 1	Method 2	Method 3	Method 4	Method 5
First metal (nm)	150	320	300	120	100
Al_2O_3 (nm)	5	5	5	5	5
Second metal (nm)	150	220	220	120	100
Gap thickness (h_{gap}) (nm)	150	320 or 35	150	120	70
Depth/width (h_{gap}/5 nm)	30	50 or 7	30	24	14
Average sidewall angle (deg)	70	77	70	73	80

view. The samples are fabricated with ALD and adhesive tapes following Chen et al.'s method,[8,14,26] which basically follows four steps (first, metallic frame formation and ALD process; second, metallic film deposition and exfoliation process) of the fabrication procedures in Sec. 2. The samples of each method are all prepared with a gap width of 5 nm, by coating the same thickness of the alumina layer with ALD gap thickness (h_{gap}) at the gap. The sidewall angle, the metallic film thickness, gap thickness (h_{gap}), and the average depth/width are measured from the cross-sectional SEM images and listed in Table 2.

3.1.1 Method 1: Tilted MIM nanogaps using AZ5206E

The cross-sectional schematics of the method 1 procedure are shown in Fig. 5(a). The fabricating conditions and parameters applied at each step are listed in Tables 1 and 2, respectively. Specifically, Cr 3 nm and Au 150 nm are deposited with an e-gun evaporator (Vacuum Tech., Korea) for the first metal frame. After the lift-off, alumina layer of 5 nm is

coated over the metal frame with ALD. The condition of using ALD is mentioned in Sec. 2.2. Third, the second metallic films of Au 150 nm without adhesion layer are deposited by e-gun evaporator again. Finally, an adhesive tape is used for the exfoliation process. The average film thickness of the first and second metallic films and the gap thickness of both metallic films are all 150 nm, showing a flat surface of the MIM nanogaps.

Top views of the SEM images are shown in Figs. 5(b) and 5(c). The dark-colored rectangular-shaped arrays (metallic film) are spaced in between the bright gray-colored surface (metallic film covered with alumina) over an area of 200 μm × 150 μm. Nanogaps that are in between the different colored sections in Fig. 5(c) can be seen by a cross-sectional SEM image [Fig. 5(d)]. The gap thickness is 150 nm, the same as the metallic film thickness. The sidewall angle of the first metallic film is 70 deg, and the schematics in Fig. 5(a) show that the reason is due to the photolithography in step 1, and that the tape-peeling process in step 4 does not matter.

3.1.2 Method 2: An asymmetric V-groove structure using AZ5214E

In this method, the first metallic frame formation are done by photolithography with photoresist AZ5214E with Cr 3 nm and Au 320 nm as in Fig. 6(a) (see Table 2). After lift-off and an alumina layer coating with ALD, a secondary metallic film is deposited at 320 nm [Fig. 6(b)] and 220 nm [Fig. 6(c)] at different samples. An adhesive tape is used for the exfoliation process. An asymmetric V-groove shape appears due to the different height of the first and second metallic films and the direction of the peel depending on the edge shape of the first metallic frame.

As shown in Fig. 6(b), the formation of an asymmetric V-groove gap shape is observed by the cross-sectional SEM images, which are taken before and after applying an adhesion tape. The first metallic frame forms a pointed tail at the bottom edges due to an undercut-shaped photoresist while depositing the Au film [see Fig. 6(b)(ii) cross-sectional view from the lift-off result]. On top of the point tail of the first Au metallic film, a cross-link composed of metallic
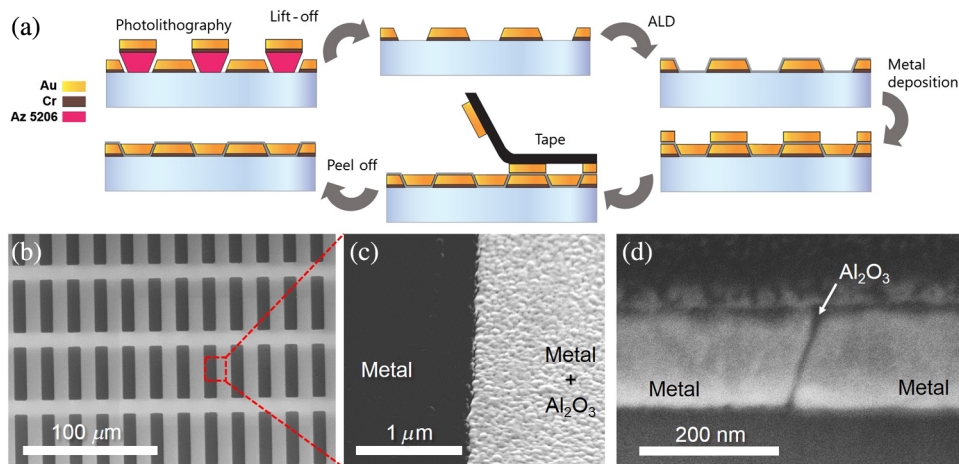

Fig. 5 (a) Cross-sectional schematics of the procedure of method 1, (b) a top view of SEM images of nanogap sample with large areas, and (c) an enlarged image of (b), focused on an alumina line of the rectangular-shaped loop in between metallic films. (d) A cross-sectional SEM image of (c).
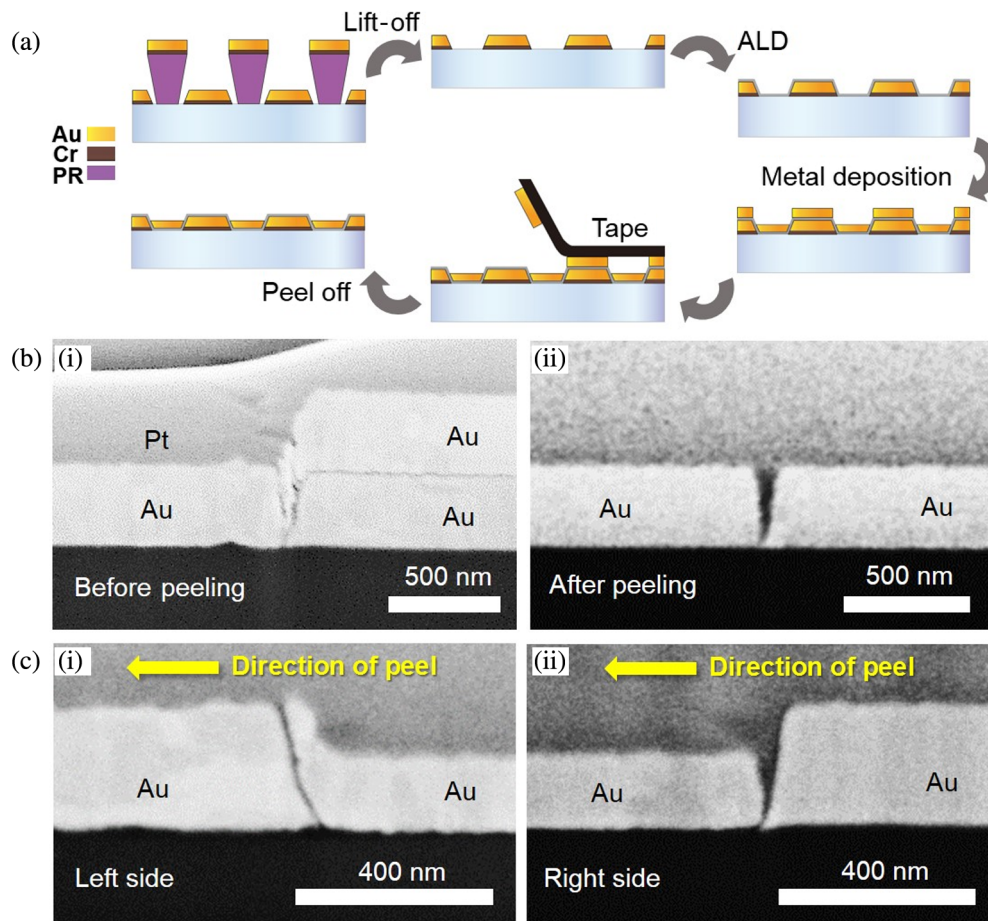
Fig. 6 (a) Cross-sectional schematics of fabricating the asymmetric V-groove type nanogap structure followed in method 2. (b) Cross-sectional SEM images of (i) before and (ii) after peeling off the unnecessary metal films that are atop of first metallic pattern. (c) Cross-sectional SEM images of (i) the left side and (ii) the right side of a single rectangular-ring shape after peeling off the unnecessary metallic films from right-to-left direction.

grains is formed, unlike in smoother secondary metallic film away from the gap region [Fig. 6(b)(i)]. These cross-linked metallic grains and the unnecessary films that are on top of the first metallic frame are removed by an adhesion tape, forming a V-groove shape of the gap [Fig. 6(b)(ii)].

When the difference of the first metallic frame and the secondary film thickness is increased to 100 nm, a tilted MIM structure and an asymmetric V-groove both appear depending on the direction of peel during the exfoliation process. The V-groove shows the gap thickness of about 35 nm, and the sidewall angle at the point tail is 60 deg while the sidewall angle of the secondary metallic film is 80 deg. As shown in Fig. 6(c)(i), the nanogap with the gap thickness of 320 nm is the same as the thickness of the first metallic frame. The cross-sectional view of SEM images that are from (i) the left and (ii) the right side of the rectangular 3 mm × 5 mm is shown in Fig. 6(c) after peeling the adhesive tape in the direction of right-to-left. A cross-link part from both SEM images in Fig. 6(c), the secondary metallic regions on top of the point tail at the first metallic film bottom edges, shows two weak-bonding points: the top [see Fig. 6(c)(i)] and bottom edge of the first metallic film [see Fig. 6(c)(ii)]. These weak-bonding points correlate with the direction of peeling and the cross-sectional slope and size of the point tail apart from the first metallic film.

For instance, the adhesion tape-peeling direction comes toward the sidewall of the first metallic frame in Fig. 6(c)(i) while the peeling direction is opposite in Fig. 6(c)(ii). Moreover, the slope of the point tail is steeper than in Fig. 6(c)(ii), and the size of the point tail is larger.

3.1.3 *Method 3: An asymmetric Y-groove structure using ion beam etching*

In method 3, an ion beam etching is added to make the first metallic frame. The argon (Ar) ion beam trims the edge of the metallic frame, including the point tail, and ends up with a thickness of 320 nm. After the ALD process, the secondary metallic film is deposited 100 nm lower than the thickness of the first metallic film. The exfoliation process is carried out by applying an adhesive tape as before. Figure 7(a) describes the fabrication procedures in a cross-sectional view.

The etching process is carried out by an Ar ion beam miller (Hitachi Tech, Ltd., Japan). The accelerating voltage is fixed at 300 V, and the Ar gas flow rate is set at 20 sccm under the pressure of 5 micron Torr. The sample is attached to the sample wafer of the mount and the Ar beam size covers 6 of 4-in. wafers as shown in Fig. 7(b). The sample mount is rotated in a clockwise direction and the target angle can be tuned by tilting the central axis of the mount. When the
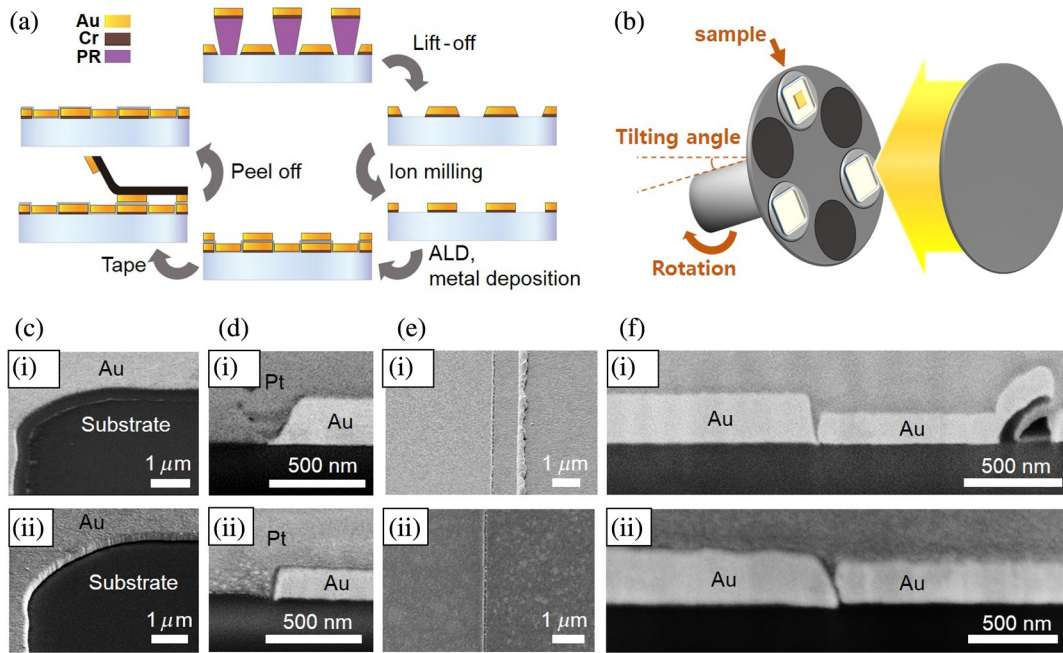
Fig. 7 (a) Cross-sectional schematics to show the procedure of nanometer gap fabrication, including ion beam etching process in method 3. (b) A schematic of a typical design of the sample mount and an ion beam source inside the Ar ion miller chamber; Ar ion beam size covers 6 of 4-in. wafers. The sample mount is connected to the axis of rotation, and it can tilt the mount angle. (c) Tilted-view and (d) cross-sectional SEM images of (i) before and (ii) after trimming the edges of the first metallic film using ion beam etching process. (e) Top-view and (f) cross-sectional SEM images that are taken after the exfoliation process followed in (i) method 2 and (ii) method 3.

tilting angle of the mount axis is set at 15 deg for 3 min and additionally set at 75 deg for 4 min, the etch depth of the Au film is about 37 nm (see Table 3). This etching process is additionally repeated three more times to remove the point-tail part of the first metallic film. The two different tilting angles are set to avoid the shadow effect and an unexpected deposition from etched metallic clusters.

The tilted and cross-sectional SEM images of (i) before and (ii) after ion beam etching are shown in Figs. 7(c) and 7(d), respectively. The point-tail part of the first metallic film is removed after etching as in Figs. 7(c). In Fig. 7(d), 250 nm of the first metallic film decreased to 100 nm, and the point-tail part is clearly removed showing the sidewall angle as 70 deg with rounder edges than in methods 1 and 2. Furthermore, the oft-existing undesired remaining

Table 3 Ion beam etching rate.

Material	Etch rate[a] (nm/min)
Au	9.1
Ag	10
Cu	4.8
Cr	1
AZ5206E	3.6

[a]The etching rate was estimated from the ion etching recipe in Sec. 3.1.3, setting the standard tilting angle as 15 deg.

photoresist layers are removed by ion beam etching as can be seen by the comparison of the top and cross-sectional view of SEM images in Figs. 7(e) and 7(f). By removing the point-tail part of the first metallic film and the undesirable remaining photoresists, a nanogap can be seen above the substrate in between the Au metallic films in the cross-sectional view of the SEM image of Fig. 7(f)(ii). The gap thickness of this MIM structure, 150 nm, is much larger than the V-groove case of Fig. 7(f)(i), where the nanogaps exist only at the bottom near the substrate.

3.1.4 *Method 4: MIM nanogaps using a photoresist mask*

The photolithography and ion beam etching are carried out on a metallic film to fabricate the first metallic frame using the photoresist AZ5206E as a sacrificial layer [Fig. 8(a)]. Etching conditions are followed as in method 3. After stripping the photoresist by acetone, ALD process, secondary film deposition and exfoliation process by tape are carried out as in method 1, 2, and 3. Unlike methods 1, 2, and 3, the thicknesses of the first and the secondary metallic films are both 120 nm with the sidewall angle of 73 deg.

Photolithography and lift-off processes (methods 1, 2, and 3) have thickness limitations because of the relation between the photoresist and an appropriate deposition thickness (see Sec. 2.1.1). For instance, AZ5206E (or AZ5214E) is used for 150 to 200 nm (or 300 to 400 nm) of metallic thickness due to a good rule of thumb.

However, the thickness limitation can be solved using the photoresist as a shadow mask, also as a sacrificial mask, for patterning the first metallic frame. As shown in Fig. 8(b), the cross-sectional view of SEM images of (i) before and (ii) after
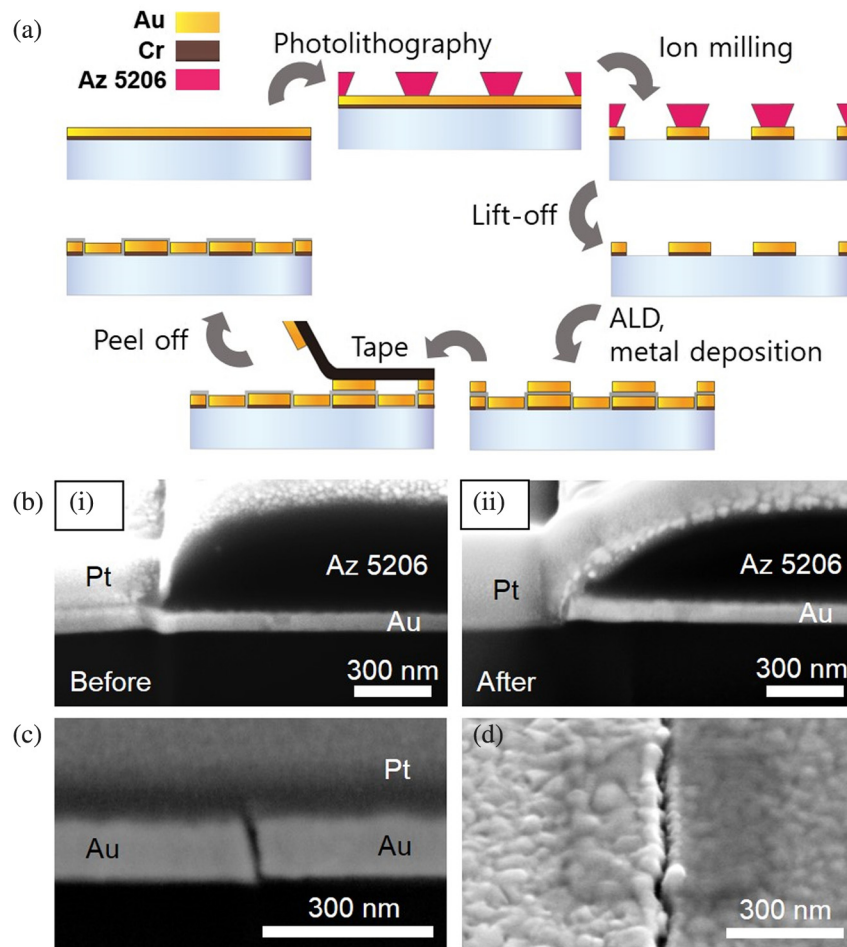
Fig. 8 (a) Cross-sectional schematics to show the procedure of method 4; AZ5206E photoresist is a shadow mask of an Ar ion beam etching. (b) Cross-sectional SEM images of (i) before and (ii) after milling Au layer through photoresist shadow mask. The Ar ion beam etches 100-nm-thick Au layer, while it etches AZ5206E photoresist about 60 nm. (c) A cross-sectional and (d) a top-view SEM image after the exfoliation process in method 4.

ion beam etching a metallic film through a photoresist mask shows the possibility of fabricating a thin metallic frame. The Ar ion beam etches the photoresist about 60 nm while etching 100-nm-thick Au film. We suspect that the Pt deposition, a protection layer while slicing the sample for a cross-sectional view, presses down the photoresist resulting in a trapezoidal shape.

Furthermore, the thickness of an edge part of the photoresist after ion beam etching is decreased by an ion beam etching and shows the maximum thickness of the metallic film with photoresist AZ5206E around 100 nm [Fig. 8(b)(ii)]. A shadow mask AZ5206E that has a smaller undercut-depth than AZ5214E is suitable for avoiding the undesired secondary deposition on the shadow region of the photoresist.

A sub-10 nm of alumina layer is sandwiched between 120-nm Au films with the sidewall angle of 73 deg as shown in a cross-sectional and a top view of the SEM image in Figs. 8(c) and 8(d), respectively. As the top edge of the first metallic frame is not rounded as in method 3, it is possible to deposit the secondary Au film with the same height as the first metallic film as in method 1 without making cross-links between the unnecessary Au films that are on top of the first metallic frame and the secondary Au film,

which is plugged in the rectangular holes of the first metallic frame.

Unlike the previous methods mentioned above, the thickness of a nanogap MIM film is a thinner version of method 1. A thin and flat nanogap metallic structure has shown advantages over the recent studies in that it can enhance the electric field stronger than a thick and/or a tapered-edge type of nanogap structure.[29]

3.1.5 Method 5: An asymmetric Y-groove structure using metallic shadow mask

In method 5, an ion beam etching process is performed through a metallic shadow mask, and the sacrificial layer is exfoliated by a chemical etchant [Fig. 9(a)]. A 100-nm-thick metallic film with Cr 3 nm of adhesion layer is prepared. Cr 5 nm–Cu 160 nm–Cr 20 nm metallic film is patterned by photolithography and lift-off. This metallic film acts as a shadow mask for an Ar ion beam to pattern the first metallic frame. After the ALD process, the secondary 100-nm-thick metallic film with an adhesion layer Cr 3 nm is deposited. Finally, the exfoliation process is performed by a chemical etchant for removing the shadow mask, which is also a sacrificial layer.
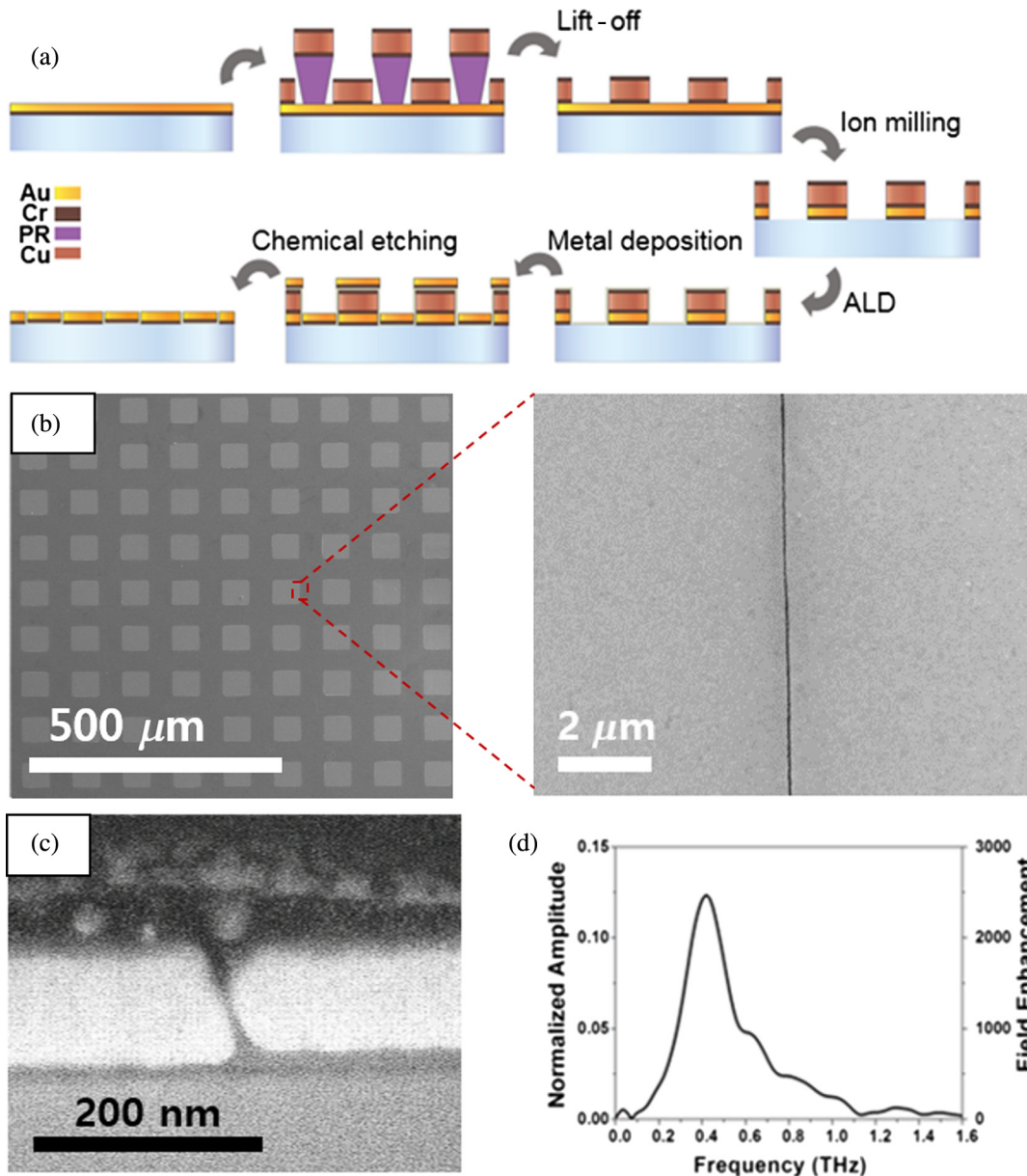
Fig. 9 (a) Cross-sectional schematics of the procedure of method 5, chemical etching instead of adhesive tapes in the exfoliation process. A patterned Cr–Cu–Cr layer is a shadow mask while using ion beam miller. (b) Top view of SEM images; a dark gray shows the remaining Cr layer on top of the first metallic frame (left); an enlarged part of the left SEM image is shown after an extra wet-etching process and ultrasonic agitation (right). (c) A cross-sectional SEM image of the sample part of (b). (d) A normalized transmitted amplitude and the FE of the sample.

The explanation of the first and the second layer of the shadow mask and the chemical etching process is given in Sec. 2.4. The top layer of the shadow mask, 20-nm Cr layer, is coated to prevent the edge of the mask film being rounded from ion beam etching. The Cr dry etching rate is 1 nm/min, which is much slower than Au (9 nm/min) and Cu (5 nm/min), so the Cr layer of the top of the shadow mask can endure while milling a thin Au film. This work is to form the sidewall angle of the first metallic frame as 80 deg [See Fig. 9(b)]. The undesired particles after wet etching are washed out by sonication in acetone.

A top view of a 50-μm × 50-μm sized square-ring array with 100-nm-thick MIM structure of the SEM image is shown in Fig. 9(b). The dark gray-colored region shows the remaining Cr layer on top of the first metallic frame that can be distinguished from the bright gray-colored square regions (secondary-deposited Au films). After an extra wet-etching and cleaning process, the enlarged SEM image of a part of the side of the ring array shows that a dark line (alumina, nanogap) passes through the bright gray (Au film) surface. This explains that the Cr layer on top of the first frame is removed.

In Fig. 9(c), a cross-sectional view of an SEM image shows the nanogap MIM structure that has minimum 5-nm gap width with the gap thickness of 70 nm. This structure has an adhesion layer, a dark gray line sandwiched between the bright gray-colored area (the substrate) and the white-colored area (the Au films). Underneath the right side of the Au film,

the gray line is thicker than the left side. This results from the two layers: an alumina layer and a Cr layer. The alumina layer is coated over the first metallic frame, including the substrate, and subsequently, the Cr layer, the part of the secondary film deposition process, is deposited.

To confirm that the sample is an optically active nanogap, the FE spectra of the sample are shown in Fig. 9(d), by estimating from normalized THz transmitted spectra. The transmitted spectrum from the sample is normalized by the spectrum of the bare substrate. Using the Kirchhoff integral formalism,[43] the enhanced field in near-field, FE, can be calculated as dividing the effective gap coverage ratio. Since the incident THz beam is polarized, the sides that are perpendicular to the incident beam strongly enhance the field inside the nanogap. Therefore, the effective gap coverage ratio can be defined as A_{gap}/A_{metal}, where A_{gap} indicates the area of the parallel sides of the square-ring arrays that are perpendicular to the incident beam and A_{metal} implies the area except the A_{gap}. As a result, up to 2700-fold FE at around 0.4-THz resonant frequency is obtained. The experimental data made from other methods are reported in Refs. 29 and 45.

The samples made by the etching method can be washed again unlike those made by an adhesive tape, because the secondary metallic film is deposited after the adhesion layer. Moreover, the exposed alumina layer on top of the first frame does not exist in this method due to the sacrificial layer. This results in a top view of nanogap ring arrays in metallic films nonexisting alumina layers and a cross-sectional view of metal/alumina/metal structure, which is the candidate for sensing biomolecules and SERS.

3.2 Cross-Sectional Electromagnetic Field Distributions in a Nanogap with Different Gap Shapes

To understand the electric FEs in the nanogap, the electric field distributions of different nanogap shapes were obtained from finite-element method simulations using COMSOL Multiphysics. The alumina layer was fixed at 5 nm and

assumed the refractive index of the alumina in the nanogap as n_{gap}, 2.12, where the substrate was set as n_{sub}, 3.4.[26,29] The dielectric parameter of the gold was approximated by the Drude model with plasma frequency of 1.37×10^4 THz and damping frequency of 40.7 THz.[16,44] The incident plane wave of a THz pulse with the center frequency of 0.4 THz is normally illuminated from the bottom of the substrate and funnels through the nanogap. The transmitted field with a nanogap structure is normalized by the transmitted field through the substrate without the structure to calculate the FE factor as in Fig. 10. Each of the geometric parameters is adopted from SEM images of Fig. 5(d) in Sec. 3.1.1, Figs. 6(b)(ii) and 6(c)(i) in Sec. 3.1.2, Fig. 7(f)(ii) in Sec. 3.1.3, Fig. 8(c) in Sec. 3.1.4, and Fig. 9(c) in Sec. 3.1.5. The sidewall angles and the gap thickness values of each case are adopted from Table 2. To focus on the effect of the gap shape, the calculated in-plane structural geometries in Fig. 10 are the same dimensions, multiple slits with a periodicity of 50 μm.

Recently, it is reported that when the nanogap width is fixed to sub-10 nm, the FE factor in the nanogap shows an increase as the gap thickness of the metallic film decreases.[29,45] For instance, among the features in Fig. 10, an asymmetric V-groove in Fig. 10(c) has the thinnest gap thickness of about 35 nm but the FE factor is 1440 reaching the largest value. On the other hand, the nanogap with the thickest gap thickness [Fig. 10(b)] shows the smallest FE factor of 320. In addition, Figs. 10(a) and 10(d) both have the gap thickness of 150 nm and show the FE factor of 590 and 570, respectively, while 120-nm-thick nanogap [Fig. 10(e)] shows 720- and 70-nm-thick nanogap [Fig. 10(f)] shows 1050. Especially, the contribution of the gap thickness to the FE factor can be found by comparing (a) and (e). Even though both cases of the sidewall angle are similar to 70 deg and the gap volume is constant, the latter one shows 130 increase of the FE factor because the thickness is 30 nm lower.

By comparing Figs. 10(a) and 10(d), the FE factor varies depending on whether the surface near the gap is tapered or nontapered even though they have the same gap thickness. In the cross-sectional view, if the thicknesses of the left and the
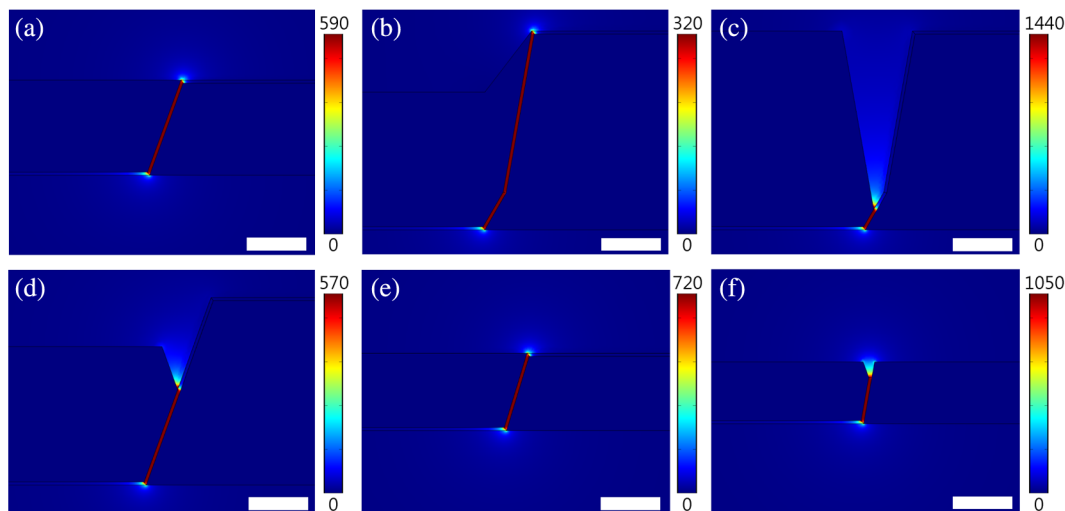

Fig. 10 The calculated cross-sectional electric field distributions for the nanogaps from (a) method 1, method 2 where (b) is a reclined-shaped nanogap and (c) is an asymmetric V-groove nanogap, (d) method 3, (e) method 4, and (f) method 5. Scale bars are 100 nm.

right metallic film around the alumina gap line are different and if they are thicker than the gap thickness [Fig. 10(d)], this is called asymmetric tapered structure and the FE factor is 20 lower than the case of the nontapered structure [Fig. 10(a)]. It seems that making the sidewall angle constant in a single nanogap as a nontapered nanogap structure is also a way to increase the FE factor besides decreasing the gap thickness. However, Figs. 10(e) and 10(f) show a nanogap structure with a thinner gap thickness but the tapered structure shows a larger increase in FE factor than the opposite case. This confirms that the gap thickness is a dominant factor in nanogap geometries to achieve strongly confined electric fields at the gap volume. Therefore, a strategy to achieve an ultimate FE is to make an asymmetric V-groove array, which is irrelevant to the thickness except for the point-tail part.

4 Conclusion

In this study, we divide the recipes into five methods depending on the results of the cross-sectional nanogap shape, while maintaining the four sequential steps of the fabrication procedure suggested from Chen et al.[26] to form MIM nanogap array structure. The selection of the photoresist material, the thickness of the metallic film, whether the exfoliation is carried out by tape or chemical etching, and the formation method of the first metallic frame, photolithography by lift-off or by ion beam etching affect the gap shape. The nanogap array is an optically functionalized MIM structure, which is shown by the transmission optical microscope image and terahertz transmission spectra. The simulated results show that the electric field enhanced volume, expressed in terms of the FE factor, differs according to the cross-sectional gap shapes.

The gap shape geometries are analyzed by the gap thickness and the sidewall angle of the metallic film at the gap from the cross-sectional SEM images. The sidewall angles of the samples are at least 70 deg except for the V-groove structure made by method 2. Regardless of the sidewall angle, the simulated results show the FE factor increasing as the gap thickness and decreases. However, when the thicknesses of the samples are the same, the one that has a constant sidewall angle in a nanogap shows more increased FE factor in the electric field distributions. Methods 1 and 2 are the simplest and the most time-efficient way to fabricate the nanogaps among the methods 1 to 5. Since the sample of method 1 has a constant sidewall angle in the nanogap, it is easy to define the average gap volume. Method 2 can obtain the largest FE factor among methods 1 to 5 by making V-grooves, but the yield is 50% because of the tape-peeling directionality. Method 3 is more complicated by adding an ion beam etching process, but it can increase the yield of a thick nanogap structure over 300 nm by removing the undesired materials, such as the existing photoresist layers after lift-off and the point-tail part of the first metallic film. Although method 4 is also more complicated than methods 1 and 2, the average thickness is thinner and it has the same structural advantages as method 1. Method 5, including chemical etching unlike the other methods, is the most time-consuming way. However, the sample of method 5 has the thinnest gap thickness among the non-V-grooves without an alumina layer on the surface and it is mechanically rigid so it can be reused. We suggest the category to fabricate the quadrangle-ring-shaped nanometer gap arrays with aimed degrees of resulting gap geometries for specific applications, such as sensing biomolecules, SERS, and nano-optical electrodes.

References

1. L. Novotny and N. van Hulst, "Antennas for light," *Nat. Photonics* **5**(2), 83–90 (2011).
2. V. Giannini et al., "Plasmonic nanoantennas: fundamentals and their use in controlling the radiative properties of nanoemitters," *Chem. Rev.* **111**(6), 3888–3912 (2011).
3. Q. Fu et al., "Highly reproducible and sensitive SERS substrates with Ag inter-nanoparticle gaps of 5 nm fabricated by ultrathin aluminum mask technique," *ACS Appl. Mater. Interfaces* **7**(24), 13322–13328 (2015).
4. Y. Yokota et al., "Essential nanogap effects on surface-enhanced Raman scattering signals from closely spaced gold nanoparticles," *Chem. Commun.* **47**(12), 3505–3507 (2011).
5. V. Flauraud et al., "Large-scale arrays of bowtie nanoaperture antennas for nanoscale dynamics in living cell membranes," *Nano Lett.* **15**(6), 4176–4182 (2015).
6. S. Aksu et al., "Plasmonically enhanced vibrational biospectroscopy using low-cost infrared antenna arrays by nanostencil lithography," *Adv. Opt. Mater.* **1**(11), 798–803 (2013).
7. Y.-G. Jeong et al., "Large enhancement of nonlinear terahertz absorption in intrinsic GaAs by plasmonic nano antennas," *Appl. Phys. Lett.* **103**(17), 171109 (2013).
8. J.-Y. Kim et al., "Terahertz quantum plasmonics of nanoslot antennas in nonlinear regime," *Nano Lett.* **15**(10), 6683–6688 (2015).
9. N. Engheta, "Circuits with light at nanoscales: optical nanocircuits inspired by metamaterials," *Science* **317**(5845), 1698–1702 (2007).
10. M. L. Juan, M. Righini, and R. Quidant, "Plasmon nano-optical tweezers," *Nat. Photonics* **5**(6), 349–356 (2011).
11. O. M. Marago et al., "Optical trapping and manipulation of nanostructures," *Nat. Nanotechnol.* **8**(11), 807–819 (2013).
12. J. Jeong et al., "High-throughput fabrication of infinitely long 10 nm slit arrays for terahertz applications," *J. Infrared Millimeter Terahertz Waves* **36**(3), 262–268 (2014).
13. K. Lee et al., "Microwave funneling through sub-10 nm nanogaps," *ACS Photonics* **3**(4), 537–542 (2016).
14. T. Kang et al., "Resonance tuning of electric field enhancement of nanogaps," *Appl. Phys. Express* **8**(9), 092003 (2015).
15. C. Genet and T. W. Ebbesen, "Light in tiny holes," *Nature* **445**(7123), 39–46 (2007).
16. M. A. Seo et al., "Terahertz field enhancement by a metallic nano slit operating beyond the skin-depth limit," *Nat. Photonics* **3**(3), 152–156 (2009).
17. F. J. García-Vidal et al., "Transmission of light through a single rectangular hole," *Phys. Rev. Lett.* **95**(10), 103901 (2005).
18. Z. Dong et al., "Second-harmonic generation from sub-5 nm gaps by directed self-assembly of nanoparticles onto template-stripped gold substrates," *Nano Lett.* **15**(9), 5976–5981 (2015).
19. D. Huigao et al., "Free-standing sub-10 nm nanostencils for the definition of gaps in plasmonic antennas," *Nanotechnology* **24**(18), 185301 (2013).
20. I.-B. Baek et al., "Electron beam lithography patterning of sub-10nm line using hydrogen silsesquioxane for nanoscale device applications," *J. Vac. Sci. Technol., B* **23**(6), 3120–3123 (2005).
21. J. K. W. Yang et al., "Understanding of hydrogen silsesquioxane electron resist for sub-5-nm-half-pitch lithography," *J. Vac. Sci. Technol., B* **27**(6), 2622–2627 (2009).
22. J. Theiss et al., "Plasmonic nanoparticle arrays with nanometer separation for high-performance SERS substrates," *Nano Lett.* **10**(8), 2749–2754 (2010).
23. H. Fredriksson et al., "Hole-mask colloidal lithography," *Adv. Mater.* **19**(23), 4297–4302 (2007).
24. S. Cataldo et al., "Hole-mask colloidal nanolithography for large-area low-cost metamaterials and antenna-assisted surface-enhanced infrared absorption substrates," *ACS Nano* **6**(1), 979–985 (2012).
25. T. Siegfried et al., "Metal double layers with sub-10 nm channels," *ACS Nano* **8**(4), 3700–3706 (2014).

26. X. Chen et al., "Atomic layer lithography of wafer-scale nanogap arrays for extreme confinement of electromagnetic waves," *Nat. Commun.* **4**, 2361 (2013).

27. V. Miikkulainen et al., "Crystallinity of inorganic films grown by atomic layer deposition: overview and general trends," *J. Appl. Phys.* **113**(2), 021301 (2013).

28. M. Liu et al., "Atomic layer deposition for nanofabrication and interface engineering," *Nanoscale* **4**(5), 1522–1528 (2012).

29. S. Han et al., "Terahertz field enhancement in asymmetric and tapered nano-gaps," *Opt. Express* **24**(3), 2065–2071 (2016).

30. J. W. Lee et al., "Terahertz transparency at Fabry–Perot resonances of periodic slit arrays in a metal plate: experiment and theory," *Opt. Express* **14**(26), 12637–12643 (2006).

31. S. I. Bozhevolnyi et al., "Channel plasmon-polariton guiding by sub-wavelength metal grooves," *Phys. Rev. Lett.* **95**(4), 046802 (2005).

32. J. Lee et al., "Plasmonic waveguide ring resonators with 4 nm air gap and $\lambda 02/15\,000$ mode-area fabricated using photolithography," *Nano Lett.* **14**(10), 5533–5538 (2014).

33. C. Chen et al., "Enhanced optical trapping and arrangement of nano-objects in a plasmonic nanocavity," *Nano Lett.* **12**(1), 125–132 (2012).

34. M. L. Juan et al., "Self-induced back-action optical trapping of dielectric nanoparticles," *Nat. Phys.* **5**(12), 915–919 (2009).

35. D. J. Beesley et al., "Sub-15-nm patterning of asymmetric metal electrodes and devices by adhesion lithography," *Nat. Commun.* **5**, 3933 (2014).

36. P. Neutens et al., "Electrical detection of confined gap plasmons in metal–insulator–metal waveguides," *Nat. Photonics* **3**(5), 283–286 (2009).

37. S. Han et al., "Colossal terahertz nonlinearity in Angstrom- and nanometer-sized gaps," *ACS Photonics* **3**, 1440–1445 (2016).

38. L.-N. Tripathi et al., "Terahertz transmission through rings of quantum dots-nanogap," *Appl. Phys. Express* **9**(3), 032001 (2016).

39. Y.-M. Bahk et al., "Electromagnetic saturation of Angstrom-sized quantum barriers at terahertz frequencies," *Phys. Rev. Lett.* **115**(12), 125501 (2015).

40. H. -R. Park et al., "High-density metallic nanogap arrays for the sensitive detection of single-walled carbon nanotube thin films," *Faraday Discuss.* **178**, 195–201 (2015).

41. A. W. Ott et al., "Al_3O_3 thin film growth on Si (100) using binary reaction sequence chemistry," *Thin Solid Films* **292**(1), 135–144 (1997).

42. J. W. Elam, M. D. Groner, and S. M. George, "Viscous flow reactor with quartz crystal microbalance for thin film growth by atomic layer deposition," *Rev. Sci. Instrum.* **73**(8), 2981–2987 (2002).

43. J. S. Kyoung et al., "Far field detection of terahertz near field enhancement of sub-wavelength slits using Kirchhoff integral formalism," *Opt. Commun.* **283**(24), 4907–4910 (2010).

44. M. A. Ordal et al., "Optical properties of the metals Al, Co, Cu, Au, Fe, Pb, Ni, Pd, Pt, Ag, Ti, W in the infrared and far infrared," *Appl. Opt.* **22**(7), 1099–1119 (1983).

45. Y.-M. Bahk et al., "Ultimate terahertz field enhancement of single nano-slits," *Phys. Rev. B* **95**(7), 075424 (2017).

Biographies for the authors are not available.